Improvement of microporous silicoaluminophosphate properties by Fe and Ti insertion for photocatalytic hydrogen generation under visible light

S. Larbaoui, H. Hentit, A. Bentouami, C. Belayachi, A. Boudjemaa, K. Bachari, M.T. Sougrati, P.E. Lippens

Improvement of microporous silicoaluminophosphate properties by Fe and Ti insertion for photocatalytic hydrogen generation under visible light

S. LARBAOUI[a,c], H. HENTIT[a], A. BENTOUAMI[a], C. BELAYACHI[a], A. BOUDJEMAA[b], K.BACHARI[b], M.T SOUGRATI[c] and P.E. LIPPENS[c]

[a] *Laboratoire de Valorisation des Matériaux, Université Abdelhamid Ibn Badis, BP 188, 27000, Mostaganem, Algérie*

[b]*Centre de Recherche Scientifique et Technique en Analyses Physico-Chimiques, Bou-Ismail CP, 42004, Tipaza, Algérie*

[c]*Institut Charles Gerhardt de Montpellier, UMR 5253 CNRS-UM-ENSCM, Pôle Chimie Balard Recherche, 1919 route de Mende, 34293 Montpellier Cedex 5, France*

Abstract

Iron- and/or titanium-containing microporous silicoaluminophosphate catalysts have been synthesized, under hydrothermal conditions, using triethylamine structure directing, to obtain the aluminophosphate five phase (AFI). These solids were characterized by X-ray diffraction (XRD), Fourier transformed infrared spectroscopy (FTIR), scanning electron microscopy (SEM), nitrogen adsorption measurements, UV-visible diffuse reflectance spectroscopy (UV-Vis-DRS) and X-ray photoelectron spectroscopy (XPS). The physico-chemical analyses have revealed that Fe- and/or Ti-containing materials have significant photocatalytic properties. Thus, they have been valorized in the photocatalytic hydrogen production from water. The reaction has been conducted, under visible radiations, and the process has been followed by photo-electrochemical characterization (PEC). Hydrogen is the only produced gas and the reaction takes place in the conduction band where water is reduced to hydrogen while the holes are entrapped using hole scavengers. The results show that our catalysts exhibit a remarkably high hydrogen evolution rate and remain stable during reuse up to at least five cycles.

Keywords: SAPO-5, Substitution, , Photocatalysis, H_2 generation.

1. Introduction

Fossil fuels in the form of coal, oil and natural gas have been used for fuel industrial technology and transportation since the industrial revolution of the 18th century. Demand for fossil fuels has increased over the years, and global energy demand is expected to double by 2050, reflecting intended population growth and industrialization in developing countries [1].

Fossil fuels, as hydrocarbons when used, emit particulate pollutants, carbon dioxide and other greenhouse gases. Pollution increases risks to human health and greenhouse gases cause global warming that threatens the stability of the Earth's climate [2]. In this context, hydrogen has proved to be a potential carrier of clean and sustainable energy to replace fossil fuels [3–5]. Hydrogen gas is almost absent in our atmosphere. It must therefore be extracted from the molecules that contain it, such as water or organic compounds. Traditional hydrogen production methods using organic compounds, currently account for more than 90% of hydrogen production but require high pressures and temperatures and the use of nonrenewable raw materials [6, 7]. Therefore, the development of clean technologies to produce hydrogen from renewable sources is very important. One of these technologies is heterogeneous photocatalysis, which has proved to be effective for producing hydrogen from water. Since Fujishima and Honda works that show the possibility to produce hydrogen from water using TiO_2 as photocatalyst [8], titanium dioxide has remained the most widely used material for a long period because of its stability, efficiency and non-toxicity [9–11] and has been proved to be an active catalyst for hydrogen production from water-methanol solutions [12].

Photocatalysts are active either under UV or visible light. TiO_2 (E_g = 3.2 eV) [13] has been the first UV active photocatalyst. Since the UV represent about 4% of solar radiation and in order to exploit the maximum amount of solar radiation which is ensured by visible radiation (45%), researchers have made modifications to TiO_2 to shift its absorption spectrum to the visible light for an optimum E_g value between 1.1 and 1.7 eV [14]. These modifications have been carried

out by combining TiO_2 with other semiconductors, by doping or impregnation to obtain novel materials such as GO-TiO_2 [15], Pt-N-TiO_2-graphene nanocomposites [16], $CuInS_2$ sensitized TiO_2 [17], CNHs/TiO_2 nanohybrid [18], Ce^{3+}-TiO_2 [19], Rh and Nb co-doped TiO_2 [20], H-doped TiO_2 [21], Ti^{3+} in anatase TiO_2 [22]. Several semiconductors have also been used for the production of hydrogen from water such as VO_2 [12], CdS [23], Fe_2O_3 [24] and transition metal containing aluminophosphates [25]. Among these photocatalysts, iron oxide (Fe_2O_3) has received a great interest due to its band gap that can absorb approximately 60% of the solar energy, its chemical stability, its low cost and its ecological and economic interest [26–29]. Nevertheless, complex transition metal catalysts tend to fuse or agglomerate and even to deform during reactions, due to their high surface energy, thus losing their initial selectivity and activity, which reduces the possibility to be reused. The challenge now is to obtain photo-catalysts containing transition metals with improved selectivity, durability, stability and longevity (recyclability). The most suitable is to combine all these properties, in addition to the catalytic and adsorbent performance, by inserting the active metals into porous solids in order to obtain hybrid and multifunctional catalysts joining both the activity and selectivity of the transition metal with high stability and easy separation of the support. Thus, and in this context of idea, the substituted microporous aluminophosphates meet well these requirements [25, 30, 31].

The microporous silicoaluminophosphate materials in the AFI (aluminophosphate five) structure phase ($SAPO_4$-5) present the advantage to be synthesized with high reproducibility. Besides, the materials have many benefits in catalysis through their achieved high order, high surface area and ability to interact with atoms, ions and molecules not only at their surfaces, but throughout the bulk giving then, satisfactory performances for species selectivity [31]. Doping $SAPO_4$-5 with Ti(IV) allows to tune the optoelectronic properties of the resulting material. Furthermore, the presence of Fe in the $SAPO_4$-5 or $TAPSO_4$-5 framework improves the redox properties of the catalysts and can shift their absorption spectra to the visible range, offering

then an optimum band gap energy [29]. Moreover, it has been shown that the presence of Fe in photo-catalysts, significantly boosts their activity by suppressing the rapid recombination of photo-generated charge carriers [32].

The aim of this study is to combine the high surface area of $SAPO_4$-5 with the optoelectronic and redox properties of titanium dioxide and iron, respectively, by doping the microporous framework with photoactive Ti(IV) and Fe (III) species. Thus, we report new iron- and/or-titanium containing microporous silicoaluminophosphates as highly efficient and stable photo-catalysts for hydrogen production from water. To prevent oxidation of water to oxygen at the valence band, several hole scavengers have been employed and, in this work, benzoic acid is used as a hole inhibitor to ensure exclusively H_2 production. On the basis of cyclic voltammetry experiments, a reaction mechanism is proposed and discussed.

2. Experimental

2.1 Catalysts synthesis

The studied materials, silicoaluminophosphate ($SAPO_4$-5), titanium-containing silicoaluminophosphate ($TAPSO_4$-5), iron-containing silicoaluminophosphate ($FAPSO_4$-5) and both iron- and titanium-containing silicoaluminophosphate ($FTSAPO_4$-5) have been hydrothermally synthesized according to the literature [33–35]. Aluminum isopropoxide (Fluka, 98%), phosphoric acid (Prolabo, 85%) and silica gel (Aldrich, 99%) have been used as sources of aluminum, phosphorus and silicon, respectively. Titanium isopropoxide (Alfa Aesar, 97%) and iron (III) chloride (MERCK, 99%) have been used as sources of metals. Triethylamine (TEA) (98%, Fluka) has been used as a templating agent. The reaction mixture has been obtained by bringing together and under stirring the different sources of elements necessary for the formation of the expected structure for few hours before adding the templating agent (scheme 1) and maintaining the stirring for 2 h. Then, the resulting gel has been transferred to a Teflon-coated autoclave for crystallization at 200°C for 24 h. The Fe containing

SAPO4-5 have been heat pre-treated for 72 h under 90°C before to promote germination and ensure good crystallization. The volume of the mixture was 60 ml which represents the 2/3 of the volume of the Teflon cup. The resultant product has been filtered and washed with distilled water then dried at 353°C overnight before being calcinated under air atmosphere at 550°C for 4 h to remove the organic matter. The gel compositions and synthesis conditions are given in Table 1

Table 1. Gel composition and preparation conditions of the materials

Sample	Synthesis gel ratios (mole)							Pre-treatment		Crystallization	
	Al_2O_3	P_2O_5	SiO_2	Fe_2O_3	TiO_2	R*	H_2O	Temp.	Time	Temp.	Time
$SAPO_4$-5	1	1	0.2	0	0	1.4	70	-	-	200°C	24h
FAPSO_4-5	0.9	1	0.2	0.1	0	1.4	70	90°C	96h	200°C	24h
TAPSO_4-5	0.9	1	0.2	0	0.1	1.4	70	-	-	200°C	24h
FTSAPO_4-5	0.8	1	0.2	0.2	0.2	1.4	70	90°C	96h	200°C	24h

* R: the structure directing (triethylamine)

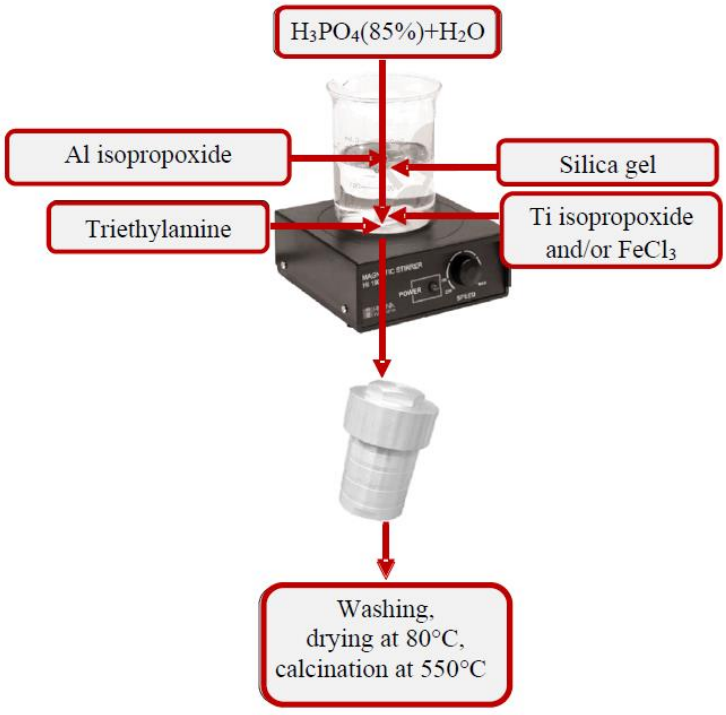

Scheme 1. Synthesis process of the catalysts

2.2. Catalysts Characterization

The synthesized photocatalysts has been characterized by different methods to determine their structural, textural and morphological properties. X-ray diffraction (XRD) analyses have been performed with a Philips X'PERT powder diffractometer in the 2θ range [2 - 90°], using monochromatic X-ray radiation provided by a copper anticathode (λ = 1.54056 Å). The measurements have been recorded with a 2θ step of 0.01° and an exposure time of 0.5 s. The Fourier transform infrared (FTIR) spectra has been recorded with an IRTF Bruker alpha spectrometer over the range 400 - 4000 cm^{-1}. The samples morphology has been observed by scanning electron microscope (SEM) using a Hitachi S4500 field effect scanning electron microscope and elemental analyses of the samples have been conducted in an attached X-ray micro analyzer. Experiments giving the adsorption-desorption isotherms of nitrogen have been carried out in a Tristar 3000 (Micromeritics. USA). Adsorption measurements require a well degassed surface. For this, the calcined sample has been placed in a Pyrex cell and out gazed at a reduced pressure (< 10^{-4} torr) at 300°C for 10 h. The cell has been then connected to the device for measurements. Isotherms has been used to calculate the BET specific surface area, microporous volume and external surface using the t-plot method. The UV-Vis diffuse reflectance spectroscopy (DRS) spectra have been obtained with a V-650 UV-VIS double-beam spectrophotometer from Jasco with integrated sphere in the 200-800 nm region. X-ray photoelectron spectroscopy (XPS) spectra have been obtained from a thermo-electron spectrometer ESCALAB 250 using a monochromatic source of Al Kα radiation (1486.6 eV) calibrated with respect to the C1s binding energy at 284.8 eV.

The electrochemical and photo-electrochemical (PEC) characterizations have been carried out at room temperature in a three-electrode cell: an auxiliary platinum electrode (Tacussel, 1 cm^2) used as a counter electrode, a saturated calomel electrode (SCE) and a working electrode (WE). The WE has first been prepared with the compressed catalyst powder in the form of pellets with

a diameter of 13 mm and a thickness of 1 mm, sintered at 200°C and then, brought into electrical contact by bonding a copper wire on its back side using silver lacquer and insulated in a glass tube with epoxy glue resin. Irradiation has been ensured by a tungsten lamp (200 W) and the PEC measurements have been performed in a Na_2SO_4 solution (0.5 M) and conducted using a potentiostat/galvanostat PGSTAT302N. The current-potential curves J(E) have been plotted at a scan rate of 0.1 $V.s^{-1}$ in the potential range (-2, +2 V) using Autolab equipment, the capacitance^{-2} vs. potential plot (C^{-2} vs.V) has been obtained at 10 kHz.

2.3 Photocatalytic hydrogen evolution

The photocatalytic experiments have been performed in a 500 mL Pyrex double-walled reactor, maintained at 50°C by a temperature-controlled bath. The solution containing Na_2SO_4 (0.5 M), benzoic acid (0.25 M) and 50 mg of catalyst has been splashed for 30 min with pure nitrogen. Afterwards the solution has been irradiated also with 3 tungsten lamps (200 W) under continuous stirring for the catalyst activation. The benzoic acid has been used as a hole scavenger preventing then the oxidation of water to oxygen. The hydrogen produced quantity has been volumetrically measured by a water manometer.

All the chemicals are analytical grade and solutions are prepared with double-distilled water.

3. Results and discussion

3.1. Characterization

3.1.1 Structural and textural properties

The XRD patterns of the four materials considered in this work are similar and the narrow line width clearly shows the high crystallinity of the samples (Fig. 1). The synthesized materials are identified to be principally in the AFI phase with a hexagonal structure and present high purity. The absence of peaks characterizing possible crystallized impurities, like silicon, titanium or iron oxides may be due to the good incorporation of those elements into the $AlPO_4$ framework

or to the formation of nanoparticles that are too small to be detected by XRD. However, there is no evidence of bulk remnant materials and impurities. There are small peak shifts to higher 2θ positions when iron and/or titanium are introduced in the $SAPO_4$-5 framework that can be related to weak variations of the cell parameters and volume although they fall within the uncertainty range of our measurements (Table 2).

Table 2. Cell parameters (standard deviations in parentheses) and average crystallite size of synthesized aluminophosphate solids.

Samples	a (Å)	c (Å)	c/a	α (°)	β (°)	γ(°)	Cell volume ($Å^3$)	Average crystallite size (nm)
$SAPO_4$-5	13.77(6)	8.44(1)	0.61	90	90	120	1386	85
$TAPSO_4$-5	13.71(2)	8.43(6)	0.61	90	90	120	1372	90
$FAPSO_4$-5	13.72(1)	8.48(9)	0.62	90	90	120	1382	99
$FTAPSO_4$-5	13.74(1)	8.42(2)	0.61	90	90	120	1376	110

The Scherrer's formula is employed to evaluate the crystallinity level of the synthesized materials. Crystalline sizes (*t*) are calculated for the five first-order reflections and the obtained values are collected in table 2. The results show that the inserted titanium and/or iron atoms increase the average crystalline size, suggesting that changes in crystallisation mechanism depend on the nature of the inserted metal.

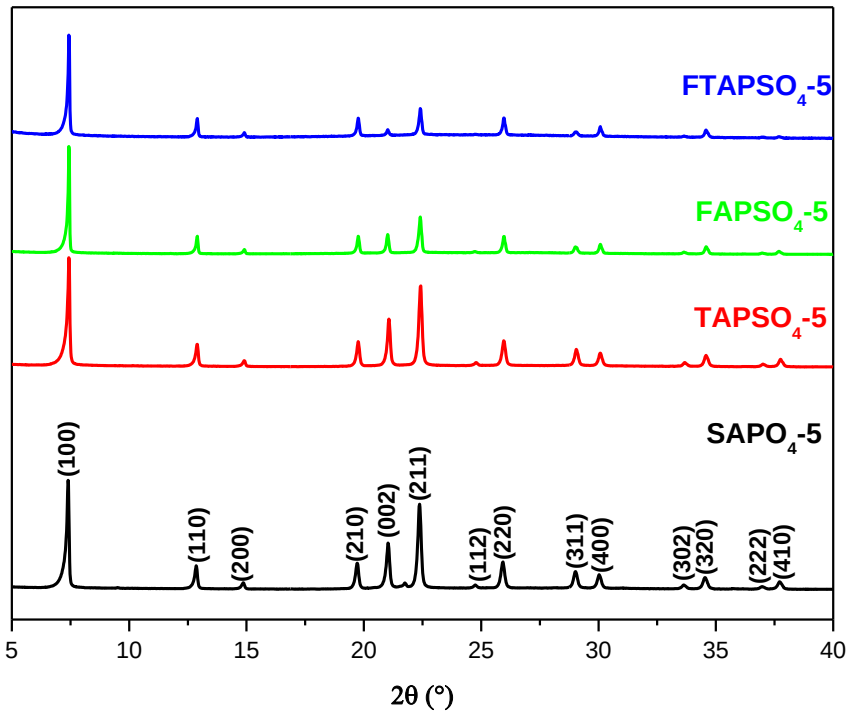

Fig. 1. Powder XRD patterns of $SAPO_4$-5, $TAPSO_4$-5, $FAPSO_4$-5 and $FTAPSO_4$-5 samples

The electron micrographs (Fig.2) show that the synthesized catalysts are well crystallized and present different morphologies when transition metals are incorporated into the silicoaluminophosphate framework. The crystals present a small size and agglomerate in various forms according to different orientations. This indicates the heterogeneous crystallization of the prepared solids during which germination takes precedence over growth. The $SAPO_4$-5 sample presents two crystalline shapes: lamellar forms aggregated into intertwined spherical clusters and hexagons agglomerated into rosebuds. The hexagonal crystallites are more flattened for the $TAPSO_4$-5 sample and agglomerate into rosettes. For the $FAPSO_4$-5 catalyst, the crystallites with hexagonal forms are oriented randomly and the composition contrast is well observed, indicating the presence of iron on the crystalline surface. The same observation is made when both iron and titanium are inserted into the $SAPO_4$-5 structure but the crystals present different morphologies taking needle forms agglomerated into bundles with different orientations.

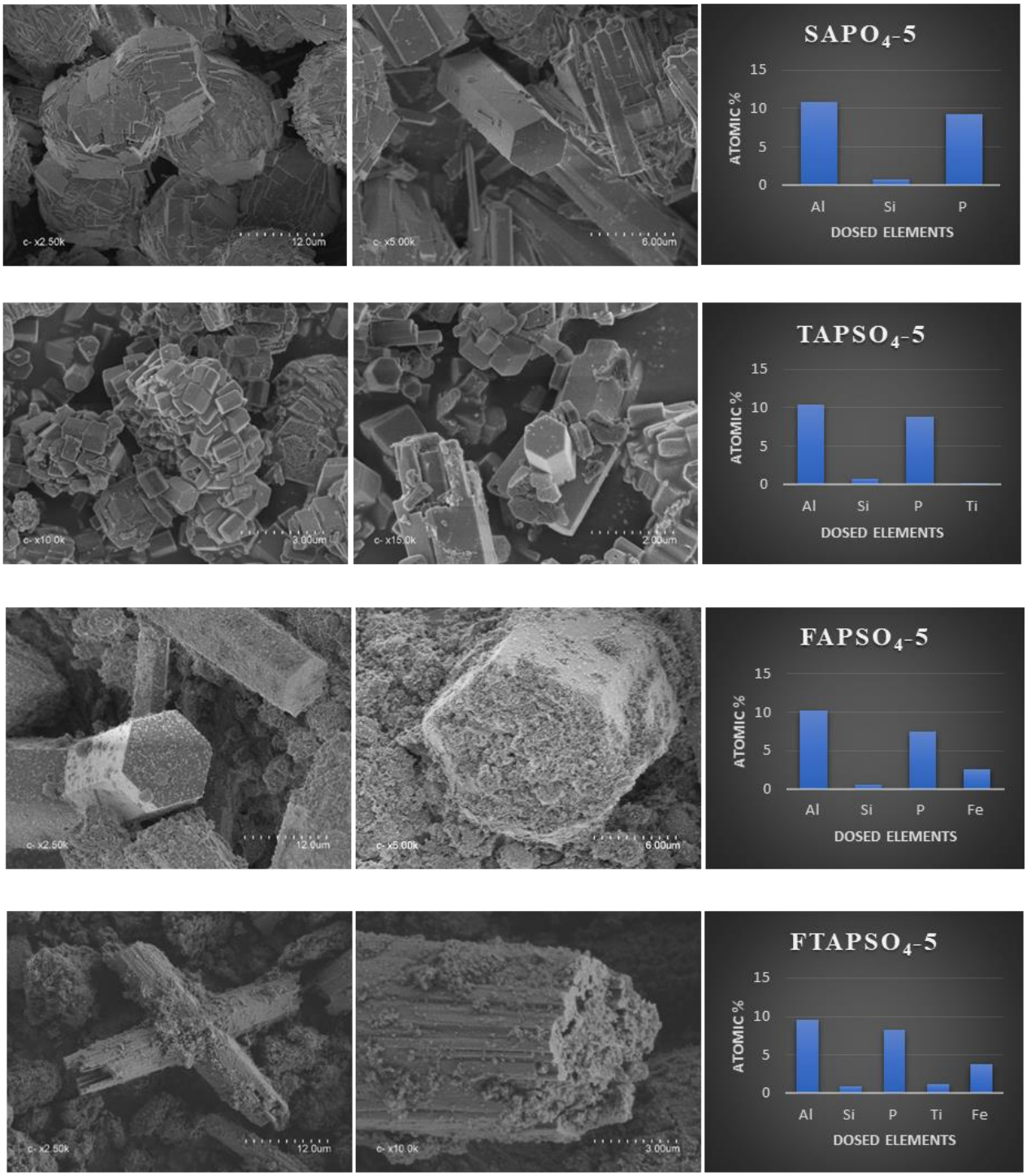

Fig.2. Electron scanning micrographs and average compositions of the prepared catalysts.

Table 3. Textural characteristics of the catalysts (standard deviations in parentheses)

Solids	BET surface area $m^2.g^{-1}$	External surface area $m^2.g^{-1}$	Microporous surface area $m^2.g^{-1}$	Micropore volume $cm^3.g^{-1}$
$SAPO_4$-5	207(2)	14(2)	193(2)	0.075(1)
$TAPSO_4$-5	264(3)	21(3)	243(3)	0.094(1)
$FAPSO_4$-5	163(2)	24(2)	139(2)	0.055(1)
$FTASPO_4$-5	149(2)	63(2)	86(2)	0.036(1)

The N_2 adsorption-desorption isotherms, displayed in Fig. S1, reveal that the four synthesized solids present a microporous texture in accordance with the type I isotherm referred to the IUPAC classification. In fact, at lower relative pressures, we notice a fast increase of the N_2 adsorbed volume which characterizes monolayer adsorption. A very slight inclination is observed on the landing, indicating a multilayer adsorption over an external surface area. At higher relative pressures, an adsorption stair is observed for the $SAPO_4$-5 and $TAPSO_4$-5 solids. The obtained isotherms have a H4 hysteresis type for $SAPO_4$-5 and $TAPSO_4$-5 and a H3 type for $FAPSO_4$-5 and $FTAPSO_4$-5, characteristic of capillary condensation through the intergranular space. From the results of table 3, we note an increase of the specific surface area and micropore volume in the case where titanium is incorporated into the $SAPO_4$-5 framework, and a decrease when iron or both iron and titanium are introduced into the framework. This evolution can be explained by the relationship between the specific surface area and the adsorption energy of the solids, which depends on the insertion rate of the metallic species in the aluminophosphate framework and their surface distribution. For iron containing catalysts, it can be predicted that the structure with the highest specific surface area can offer more catalytically active sites and, therefore, presents the best efficiency.

The bulk and surface chemical compositions of the different samples were determined by EDX and XPS, respectively (Table 4). All the expected elements were detected but there are some differences with the expected composition based on the molecular amounts of precursors used for the syntheses as reported in Table 1. The relative amount of Al evaluated by EDX is higher than expected while the P amount is lower, suggesting lower cationic charge and eventual existence of O vacancies, especially in Fe-based catalysts. The relative amount of Fe is higher than expected, which can be beneficial for catalyst properties. The amount of Si is as expected in bulk but higher at surface, while the evaluation of the weak amounts of Ti is not reliable.

Table 4. Chemical compositions obtained by XPS and EDX compared with the expected chemical formulae of the synthesized materials.

Samples	Chemical composition from XPS					Chemical composition from EDX					Cationic charge*	Expected formula**
	Al	P	Si	Ti	Fe	Al	P	Si	Ti	Fe		
$SAPO_4$-5	0.45	0.42	0.13	-	-	0.52	0.45	0.04	-	-	4.0	$Si_{0.048}Al_{0.476}P_{0.476}O_2$
$TAPSO_4$-5	0.49	0.40	0.08	0.02	-	0.52	0.44	0.04	0.003	-	3.9	$Si_{0.048}Ti_{0.024}Al_{0.434}P_{0.482}O_2$
$FAPSO_4$-5	0.52	0.38	0.07	-	0.04	0.49	0.37	0.03	-	0.11	3.8	$Si_{0.048}Fe_{0.048}Al_{0.428}P_{0.476}O_2$
$FTASPO_4$-5	0.48	0.42	0.05	0.003	0.05	0.40	0.35	0.04	0.05	0.16	3.8	$Si_{0.046}Fe_{0.09}Ti_{0.046}Al_{0.364}P_{0.455}O_2$

*Cationic charge obtained by considering Al^{3+}, P^{5+}, Si^{4+}, Ti^{4+} and Fe^{3+}

**Deduced from the gel composition (Table 1)

The binding energies of the 2p core levels of Al, P, Si, Ti and Fe obtained by XPS are similar for all the catalysts and are typical of Al^{3+}, P^{5+}, Si^{4+}, Ti^{4+} and Fe^{3+} bonded to O atoms in tetrahedral environments (Table S1) [36–42]. The observed broadened peaks for these spectra can be related to the distribution of different types of cations in the second coordination shells (Fig. S2).

The FTIR spectra of the studied catalysts, given in Fig. 3, allow us to ensure that the organic matter is totally evacuated from the solids after calcination. Indeed, the branches at 2800-3000 cm^{-1} and 1300-1400 cm^{-1}, characteristic of C-H bonds, are non-existent. In the obtained spectra, the wide absorption band, observed at approximately 3441-3610 cm^{-1} is assigned to the surface hydroxyl groups that may be bonded to Ti, Fe, Al and P atoms [43–45]. A slight increase in the intensity of this band is observed with the insertion of Ti and Fe in the $SAPO_4$-5 framework. However, this band can also be ascribed to the silanol groups (SiOH) [46]. Wide and low-absorbent band observed at 1637-1662 cm^{-1} is attributed to the O-H stretching mode [25] and can reveal the existence of adsorbed water molecules [44]. The intense band at 1100-1128 cm^{-1}, present in all the samples, is due to the symmetrical and asymmetrical vibrations of the triple degenerated phosphate (P–O) bonds and the band observed at 475 cm^{-1} is attributed to the triple degenerated bending vibration of the O–P–O bond in the PO_4^{3-} tetrahedron [47–49]. All the prepared catalysts show an absorption band at approximately 711 cm^{-1} due to the stretching

vibrations of the Al–O and P–O bonds, and possibly Me–O bonds for the MeSAPO samples [47, 50, 51]. Thus, the FTIR spectra of the prepared solids indicate clearly that the bending vibrations of hydroxyl and phosphate groups in the above-mentioned range are influenced by the nature of the transition metal. These bands shift to lower wavenumbers when the atomic number of the metal increases.

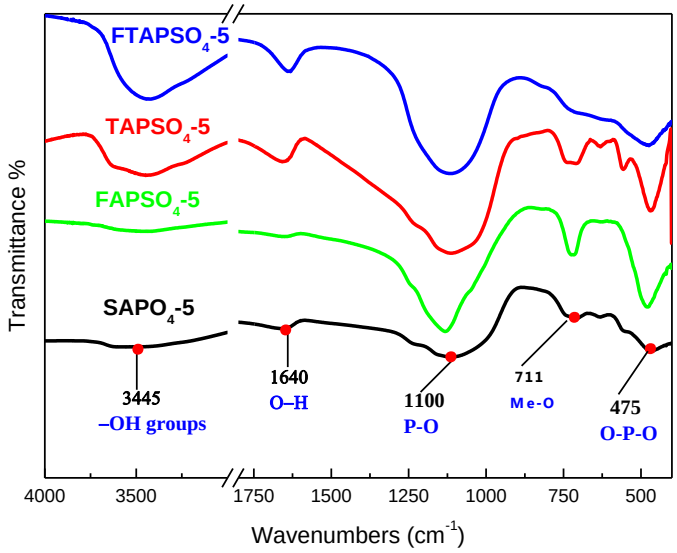

Fig. 3. FTIR spectra of the prepared catalysts and attribution of the main peaks with wavenumbers in cm^{-1}.

The UV-visible DRS is used to determine the coordination of incorporated iron and titanium atoms in the SAPO framework. The spectra of the titanium and/or iron containing silicoaluminophosphates (Fig. 4) have a common band at 220 nm, usually assigned to tetrahedral aluminium atoms, arising from Al−O charge transfer transitions [52, 53]. The position and the intensity of this band are related to different parameters such as aluminium and oxygen charge density, Al-O distances and the crystallographic position of aluminium atoms in the structure. For the titanium containing solids ($TAPSO_4$-5 and $FTAPSO_4$-5), the spectra show a band absorption at 260 nm assigned to charge transfer between Ti^{4+} and O ligands, indicating the presence of isolated tetrahedral titanium. This allows us to confirm the incorporation of titanium in the $SAPO_4$-5 framework [43, 54,55]. Moreover, the absence of band at 300-350 nm in the spectra of titanium containing solids suggests there is no anatase-like titanium oxide extra

framework [45]. Iron containing catalysts spectra show an absorption band at 260 nm assigned to charge transfer between O ligands and metal Fe^{3+} involving isolated Fe(III) framework [56–58]. In addition, the bands observed at 290 and 340 nm, showing higher intensity for the $FTAPSO_4$-5 solid, are assigned to forbidden d-d transitions of Fe(III) in distorted tetrahedral coordination [59], confirming the introduction of Fe(III) in the synthesised $FAPSO_4$-5 and $FTAPSO_4$-5 solids. Beside these intense bands, a slight shoulder is observed at 470 nm, suggesting the presence of a minor portion of octahedral Fe (III). In this case, octahedral symmetry can be achieved only if the Fe^{3+} ions are present in the lattice defect sites that are coordinated to both the bridging lattice oxygen atoms and the terminal oxygen atoms resulting from bond rupture and ligand coordination [35]. However, the presence of nanoscopic extra-framework iron species cannot be excluded, forming Fe_2O_3-like domains originating from the migration of four-coordination iron atoms from the framework when calcined in air at high temperature [59].

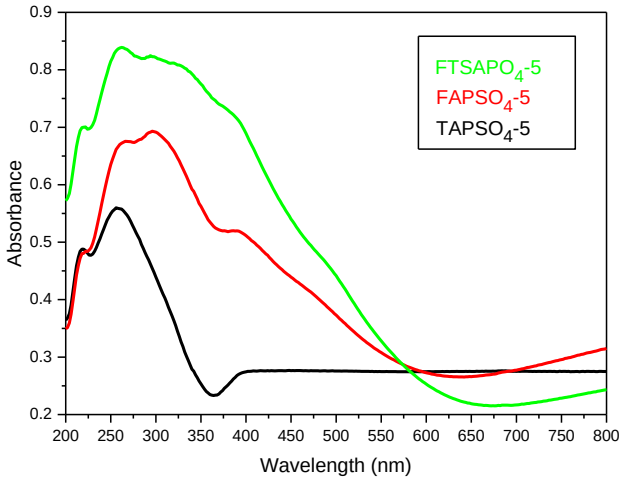

Fig. 4. UV-Vis absorption spectra of the photocatalyst samples.

3.1.2 Optical and photo-electrochemical properties

The optical properties of the catalysts are studied by UV–Vis DRS spectra. It is clearly observed from Fig. 4 that only iron containing catalysts exhibit visible range absorption.

The absorption coefficient (α) is obtained from reflectance using the Kubelka-Munk (K-M) equation [60]. Thus, data of diffuse reflectance are related to both the energy of incident photon

(hν) and the band-gap energy, E_g, according to the following equation [61,62]:

$$F(R).h\nu = \frac{A}{S}(h\nu - E_g)^n \quad (1)$$

where A is a constant depending on the properties of the studied solid and the (e^-/h^+) mobility, and n represents the transition type (n = 2 for a direct transition and n = 0.5 for an indirect transition). It is demonstrated (supplementary data) that $TAPSO_4$-5 presents a direct gap and Fe containing $SAPO_4$-5 presents an indirect gap. The curves $(\alpha h\upsilon)^2$ and $(\alpha h\upsilon)^{0.5}$ vs. hυ are shown in Fig. S6. The band gap energy for the catalysts is evaluated from the intersection of the linear region of the plot with the x-axis. Thus, the E_g values for $TAPSO_4$-5, $FAPSO_4$-5 and $FTAPSO_4$-5 are 4.05, 2.08 and 1.65 eV respectively. The decrease of the band gap value compared to bulk $AlPO_4$-5 (E_g = 5.7 eV) [63] is probably due to the presence of impurity bands induced by the partial substitution of Fe, Al and Si for Al and/or P. The band gap values of the iron containing materials suggest strong photocatalytic efficiency under visible radiations.

Fig. 5 shows the cyclic voltammogram (CV) of $FAPSO_4$-5 and $FTAPSO_4$-5 recorded at a scan rate 10 mV/s in the range [–2V, +2V]. A good electrochemical stability of the material is observed with a dark current (J_d) less than 2 mA/cm^2. The voltammogram exhibits two reversible redox peaks at -0.98 and +0.53 V vs. SCE for $FAPSO_4$-5, and at -0.80 and +0.66V for $FTAPSO_4$-5, assigned to the Fe^{+2}/Fe^{+3}redox process [64]. For $FTAPSO_4$-5, other reversible redox peaks are observed at -0.43 and +0.86 V vs. SCE probably due to the Ti^{4+}/Ti^{3+} couple [65]. The increase of the photo-current (J_{ph}), along the anodic region, indicates a *n*-type conductivity where the electrons are the majority carriers (Fig. 5). Furthermore, the sharp increase in the current below -1 V is associated with the reduction of water to hydrogen (appearance of gas bubbles on the electrode) according to the following reaction [27]:

$2\ H_2O + 2\ e^- \rightarrow H_2 + 2\ OH^-$ E= -0.14 V (-0.16 V) vs. SCE for $FAPSO_4$-5 ($FTAPSO_4$-5)

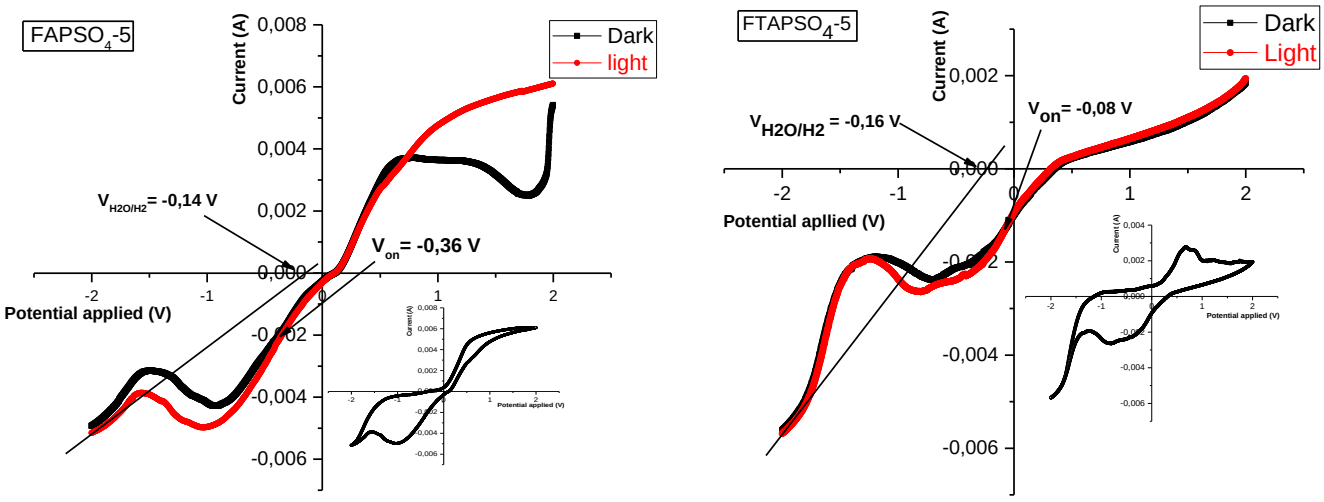

Fig. 5. Photocurrent-potential curves of $FAPSO_4$-5 and $FTAPSO_4$-5photocatalysts in the dark and under illumination.

Moreover, we can see from the CV curves that $FAPSO_4$-5 presents a lower onset potential V_{on} (-0.36 V) compared with $FTAPSO_4$-5(-0.08 V), which allows us to predict a better photocatalytic activity for $FAPSO_4$-5 [66].

To discuss the semiconducting properties of the studied solids, the Mott-Schottky spectra were investigated (Figure 6):

$$\frac{1}{C^2} = \frac{2}{\varepsilon\varepsilon_0 e N_D}\left(V - V_{fb} - \frac{KT}{e}\right)$$

The plots of C^{-2} against potential V (Fig. 6) present a linear evolution with a positive slope indicating n-type conductivity [67]. The flat band potentials, V_{fb}= -0.28 and -0.73 V for $FAPSO_4$-5 and $FTAPSO_4$-5, respectively, were determined from the abscissa at the origin of the Mott-Schottky plots. The difference between the values of V_{fb} and V_{on} indicates the existence of surface states within the band gap and indirect transitions, which is in accordance with the DRS results.

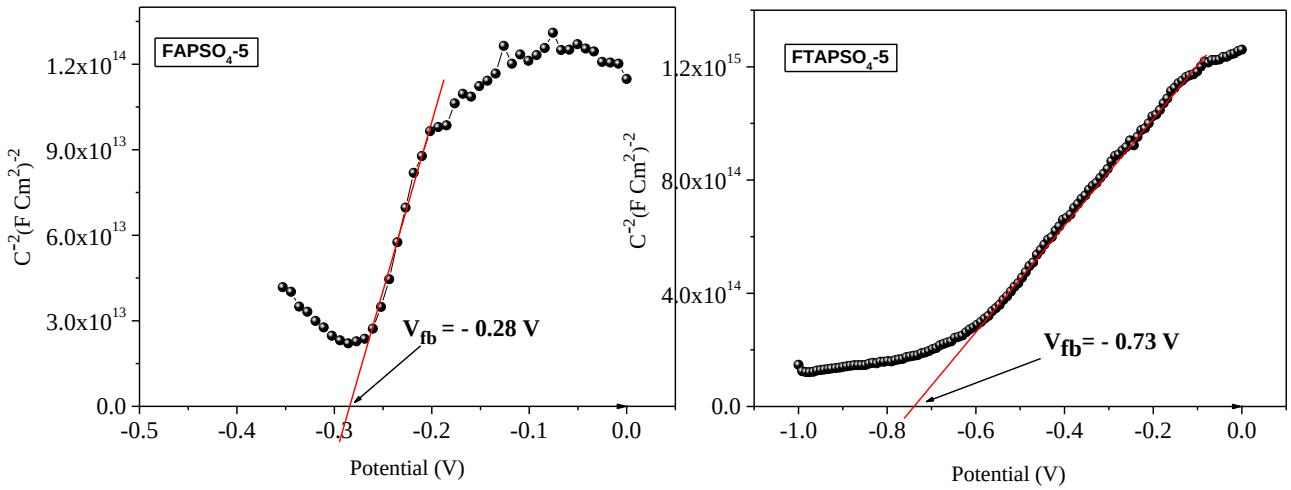

Fig. 6. Mott-Schottky curves of $FAPSO_4$-5 and $FTAPSO_4$-5 catalysts.

3.2 Photocatalytic performance of the prepared catalysts

The photocatalytic efficiency of iron and/or titanium-based silico-aluminophosphates in water splitting experiments was studied under visible light in Na_2SO_4 electrolyte with benzoic acid (BA) as a hole scavenger. When the experiments were conducted in dark, no reaction was observed and no gas was emitted, which proves that the process is indeed photocatalytic. Because of its large band gap, the $TAPSO_4$-5 solid is inefficient under visible radiation. Thus, the reaction is conducted under UV radiations at 245 and 365 nm. The best performance of the catalyst is obtained under 365 nm (Fig. 7 (a)) and this shows the dependence of the process upon the radiation wavelength. According to the data obtained for $FAPSO_4$-5 and $FTAPSO_4$-5 catalysts in Fig. 7 (b), we can note that H_2 generation starts immediately upon light irradiation of the system and the produced H_2 quantity increases very significantly to reach 65 $mmol.g_{cat}^{-1}$ with $FAPSO_4$-5 and 16.8 $mmol.g_{cat}^{-1}$ with $FTAPSO_4$-5 after 1 h. For $FAPSO_4$-5, the H_2 evolution rate increases rapidly during the first 5 min and the stabilisation at 71 $mmol.g^{-1}.h^{-1}$ is observed after 10 min reaction (Fig. 7 (c)). The same observation can be made for the $FTAPSO_4$-5 photocatalyst where the rate achieves 38 $mmol.g^{-1}.h^{-1}$ after 5 min reaction and then decreases slightly until stabilisation at 20 $mmol.g^{-1}.h^{-1}$ after 45 min of reaction process.

Hole scavenger process prevents the (e^-/h^+) recombination permitting exclusively hydrogen production in the water splitting reaction and protects the photo-catalysts against photo-corrosion [68]. The effect of the nature of the hole scavenger on hydrogen production is investigated by conducting the reactions in the presence of Na_2SO_3, BA and methanol. The obtained results are presented in Fig. 7(d) and show that the highest hydrogen production is obtained in the presence of BA for iron-containing catalysts, which is probably due to the COOH functional groups. The efficiency of BA as a hole scavenger has been shown in previous studies [68, 69] and is probably due to the partial dissociation of BA, which can give the ability enhancement of electron donation to scavenge the photo-generated holes and also for providing more quantity of protons in the solution to perform the proton reduction reaction for hydrogen production [70]. On the other hand, the pH of the solution has an important role during the photocatalytic process since it affects the surface of the photocatalyst and the charge of the subtract while the formation of benzoates under herein employed concentrations decreases the pH value of the aqueous solution to 3.2. It has been reported that pH values close to 3 are the best to promote transfer of charge from ligand to transition metal atoms (Fe or Ti) enhancing thus, the holes trapping effect [71, 72].

The stability and the recycling capacity were investigated for the $FAPSO_4$-5 photocatalyst that exhibits the best efficiency in H_2 production. Thus, the reaction was repeatedly conducted for five cycles by renewing the aqueous solution of BA, and hydrogen production was measured during one hour cycle under illumination. The evolved H_2 amount reaches 65 $mmol.g^{-1}$ in the first cycle, eventually slightly increases to 70 $mmol.g^{-1}$ in the third cycle and then decreases to 63 $mmol.g^{-1}$ in the fifth cycle, indicating that the activity of the studied photocatalyst does not show significant decrease within five cycles (Fig. 8). These results confirm the high activity and robustness of the $FAPSO_4$-5 photo-catalysts compared with the other catalysts of the present work under the same conditions. To the best of our knowledge, the obtained hydrogen

evolution rate observed for $FAPSO_4$-5 is the highest reported value. As shown in Table S5, with the lowest catalyst concentration, our material gives the best performance in term of activity and stability.

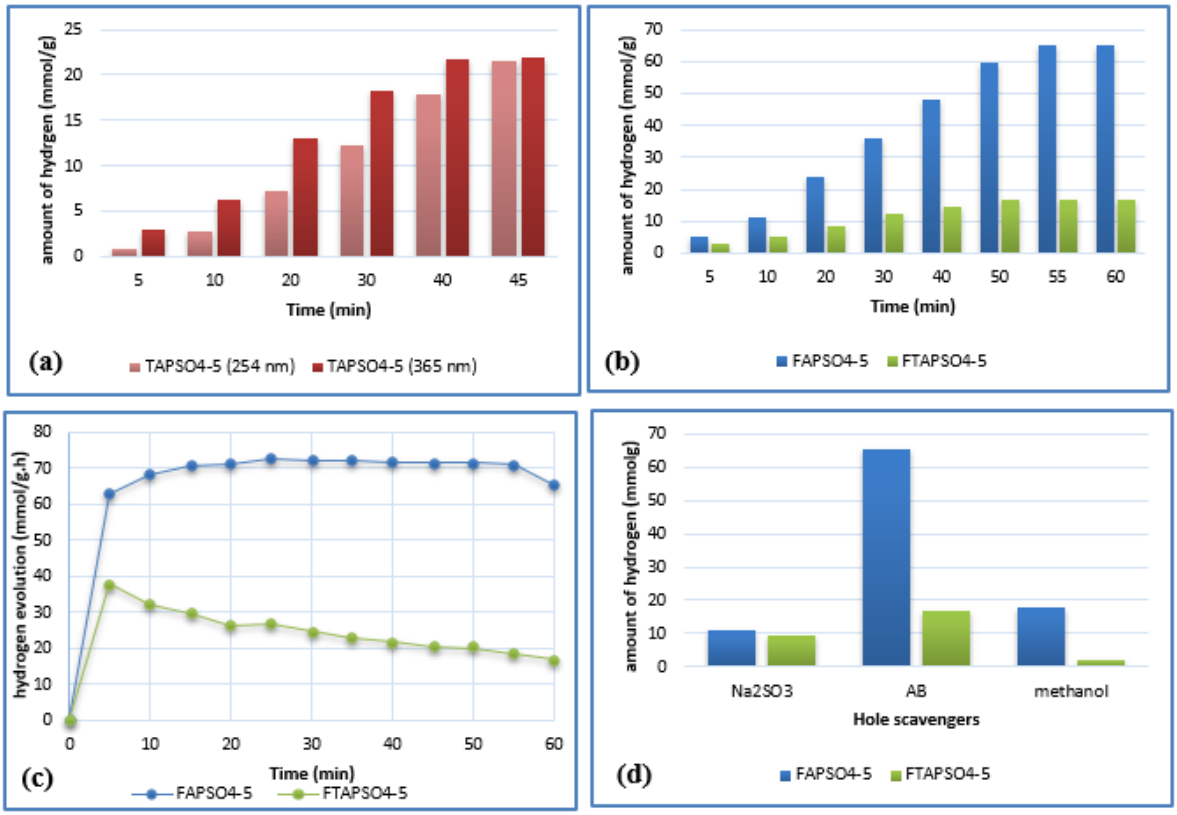

Fig. 7. (a) Hydrogen emission in the presence of $TAPSO_4$-5 catalyst under UV radiation; (b) hydrogen evolution amount in the presence of $FAPSO_4$-5 and $FTAPSO_4$-5 catalysts under visible radiation; (c) hydrogen evolution rate in the presence of $FAPSO_4$-5 and $FTAPSO_4$-5 catalysts under visible radiation; (d) effect of the nature of the hole scavenger (1h reaction time)

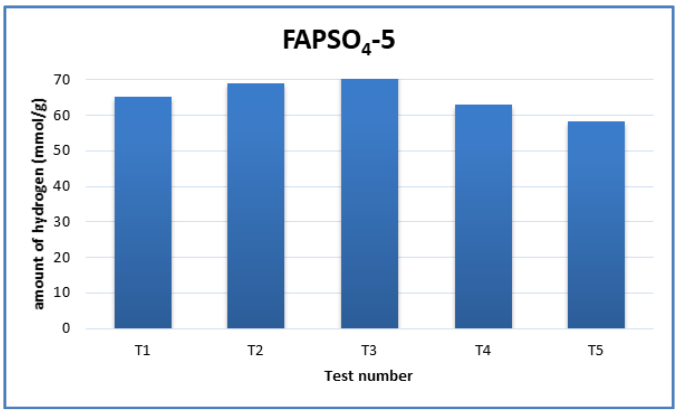

Fig. 8. Recycled performance of $FAPSO_4$-5 for hydrogen evolution (1h reaction time, BA as hole scavenger)

To explain the catalyst efficiency and the reaction mechanism, the band structures of the iron-containing catalysts are examined using our observed values of the flat band potential (E_f) obtained from the Schottky plot (Figure 6) and the band gap energy values (E_g) deduced from the Tauc plot (Figure S6). Principally, for n-type semiconductors, the Fermi level, E_f, is within the impurity band located just under the bottom of the conduction band, E_c, and the difference $\Delta E = E_c - E_f$ is assumed to be 0.1 eV for iron oxide complexes when the conductivity is lower than 10 $\Omega^{-1}.cm^{-1}$ [73], which is generally the case for iron-containing microporous zeolites [74]. Therefore, the conduction band potential of $FAPSO_4$-5 and $FTAPSO_4$-5 can be estimated at -0.38 and -0.83 V vs. SCE respectively. Associating the band gap values, the valence band potentials are estimated at 1.7 and 0.82 V vs. SCE for $FAPSO_4$-5 and $FTAPSO_4$-5, respectively.

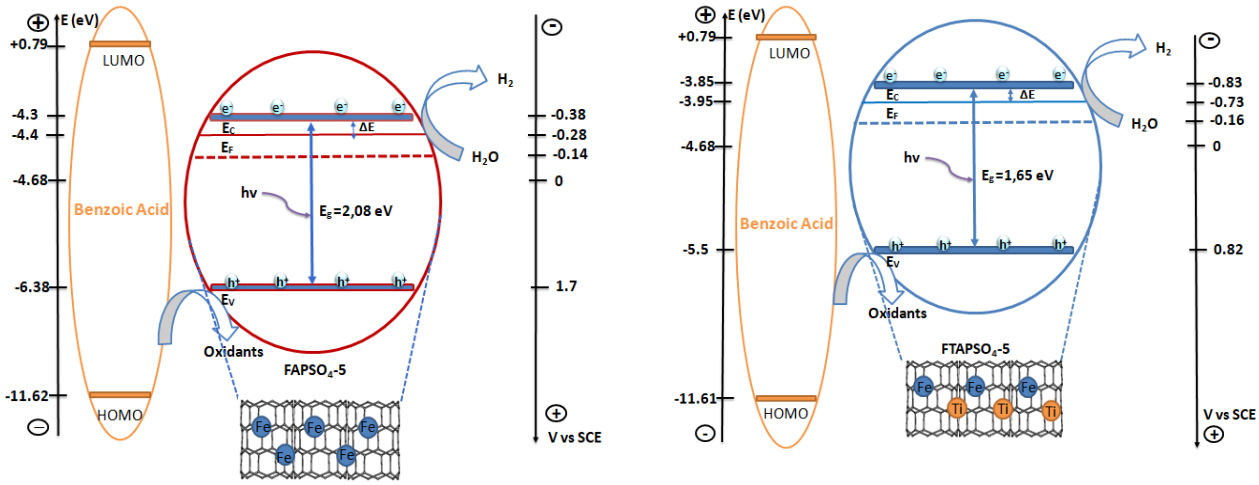

Scheme 2. Charge transfer mechanism for hydrogen evolution under visible radiation with $FAPSO_4$-5 and $FTAPSO_4$-5 photocatalysts. E_V, E_C, E_F, E_g denote the energies of the top of the valence band, the bottom of the conduction band, the Fermi level and the band gap, respectively.

Based on the mentioned results, the proposed photo-evolution hydrogen mechanism is elucidated in scheme 2 for $FAPSO_4$-5 and $FTAPSO_4$-5. Electron-hole pairs are photogenerated once the photocatalyst is excited with visible light. At the top of the valence band, the holes are inhibited with BA (as hole scavenger) to avoid oxygen formation from water oxidation while at the bottom of the conduction band the electrons react either with H^+ or H_2O to form hydrogen

(H_2). The redox ability of the catalyst can be improved when the potential vs. SCE of its conduction band minimum is more negative and that of the valence band maximum is more positive, but an excessively large band gap will reduce the light absorption [66]. Thus, the highest light energy conversion efficiency can be obtained only when a reasonable balance between the band gap and the position of the energy band edges is achieved. Moreover, in the photoelectrochemical H_2 production, low photoelectrode potential, V_{on}, promotes an efficient kinetic of the redox reaction on the electrode surface. Besides, an increase in the surface area could provide more active sites. All these factors explain the better efficiency of $FAPSO_4$-5 compared to $FTAPSO_4$-5.

4. Conclusion

In this study, we have proposed iron- and/or titanium-containing silico-aluminophosphates as novel and efficient catalysts for H_2 produced by water splitting process with visible light. A hydrogen evolution rate up to 71 $mmol.g^{-1}.h^{-1}$ was obtained, which is, as far as we know, the highest reported value in the literature. By combining different physico-chemical characterization methods, we have explained the high H_2 production in the presence of the $FAPSO_4$-5 catalyst. Investigations based on a photo-electrochemical analysis have contributed to describe the semiconducting properties of the catalysts and the charge transfer mechanism over its surface. This work also reveals the stability of the $FAPSO_4$-5 catalyst that can be reused up to 5 times.

Acknowledgements

The authors are grateful to Campus France through the PHC-Tassili program in this collaborative project N°19MDU205 and the General Direction for Scientific Research and Technological Development DGRSDT (Algeria) for their financial support.

References

[1] D. Manoj, M. Naushad, M.M. Khan, A.F. Lee, M.A. Gracia-Pinilla, R. Saravanan, F. Gracia, J. Qin, Mechanothermal synthesis of Ag/TiO_2 for photocatalytic methyl orange degradation and hydrogen production, Process Saf. Environ. Prot. 120 (2018) 339–347. https://doi.org/10.1016/j.psep.2018.09.015.

[2] M.J. Rivero, O. Iglesias, P. Ribao, I. Ortiz, Kinetic performance of TiO_2/Pt/reduced graphene oxide composites in the photocatalytic hydrogen production, Int. J. Hydrogen Energy. 02 (2018) 101–109. https://doi.org/10.1016/j.ijhydene.2018.02.115.

[3] S. Ray, J.A. Lalman, F. Arefi-Khonsari, H. Fakhouri, T. Peng, F. Saadat Ghareh Bagh, J. Zhang, Optimizing one-dimensional TiO_2 for photocatalytic hydrogen production from a water-ethanol mixture and other electron donors, J. Environ. Chem. Eng. 7 (2019) 102868. https://doi.org/10.1016/j.jece.2018.102868.

[4] D.A. Tryk, A. Fujishima, K. Honda, Recent topics in photoelectrochemistry: Achievements and future prospects, Electrochim. Acta. 45 (2000) 2363–2376. https://doi.org/10.1016/S0013-4686(00)00337-6.

[5] J.A. Turner, A realizable renewable energy future, Science. 285 (1999) 687–689. https://doi.org/DOI: 10.1126/science.285.5428.687.

[6] J. Dufour, D.P. Serrano, L.G. Jose, J. Moreno, A. Gonz, U. Rey, J. Carlos, Hydrogen Production from Fossil Fuels : Life Cycle Assessment of Technologies with Low Greenhouse Gas Emissions, Energy & Fuels. 25 (2011) 2194–2202. https://doi.org/https://doi.org/10.1021/ef200124d.

[7] R.M. Navarro, M.A. Peña, J.L.G. Fierro, Hydrogen Production Reactions from Carbon Feedstocks: Fossil Fuels and Biomass, Chem. Rev. 107 (2007) 3952–3991. https://doi.org/10.1021/cr0501994.

[8] A. Fujishima, K. Honda, Electrochemical Photolysis of Water at a Semiconductor Electrode, Nature. 238 (1972) 37–40. https://doi.org/10.1038/238038a0.

[9] Y. Lan, Y. Lu, Z. Ren, Mini review on photocatalysis of titanium dioxide nanoparticles and their solar applications, Nano Energy. 2 (2013) 1031–1045. https://doi.org/10.1016/j.nanoen.2013.04.002.

[10] S. MiarAlipour, D. Friedmann, J. Scott, R. Amal, TiO_2 /porous adsorbents: Recent advances and novel applications, J. Hazard. Mater. 341 (2018) 404–423. https://doi.org/10.1016/j.jhazmat.2017.07.070.

[11] C. Chawengkijwanich, Y. Hayata, Development of TiO_2 powder-coated food packaging film and its ability to inactivate Escherichia coli in vitro and in actual tests, Int. J. Food Microbiol. 123 (2008) 288–292. https://doi.org/10.1016/j.ijfoodmicro.2007.12.017.

[12] Y. Wang, Z. Zhang, Y. Zhu, Z. Li, R. Vajtai, L. Ci, P.M. Ajayan, Nanostructured VO_2 Photocatalysts for Hydrogen Production, ACS Nano. 2 (2008) 1492–1496. https://doi.org/https://doi.org/10.1021/nn800223s.

[13] A. Suligoj, I.A. Con, M. Mazaj, G. Drazic, D. Arcon, P. Cool, U.L. Sstangar, N.N. Tusar, Surface modified titanium dioxide using transition metals: nickel as a winning transition metal for solar light photocatalysis, J. Mater. Chem. A. 6 (2018) 9882–9892. https://doi.org/10.1039/c7ta07176k.

[14] N. Helaili, G. Mitran, I. Popescu, K. Bachari, I.C. Marcu, A. Boudjemaa, Photoelectrochemical properties of AFe_2O_4 (A = Co, Cu, Zn) ferrospinels for water photo-reduction, J. Electroanal. Chem. 742 (2015) 47–53. https://doi.org/10.1016/j.jelechem.2015.01.018.

[15] B.C. Hernández-Majalca, M.J. Meléndez-Zaragoza, J.M. Salinas-Gutiérrez, A. López-Ortiz, V. Collins-Martínez, Visible-light photo-assisted synthesis of GO-TiO_2 composites for the photocatalytic hydrogen production, Int. J. Hydrogen Energy. 44 (2018) 12381–12389. https://doi.org/10.1016/j.ijhydene.2018.10.152.

[16] M.W. Kadi, R.M. Mohamed, Preparation and characterization of Pt, N-TiO_2-graphene

nanocomposites for hydrogen production, Ceram. Int. 45 (2019) 6058–6065. https://doi.org/10.1016/j.ceramint.2018.12.077.

[17] H. Shi, C. Wang, E. Liu, X. Hu, J. Fan, Y. Yan, M. Yang, $CuInS_2$ sensitized TiO_2 for enhanced photodegradation and hydrogen production, Ceram. Int. 45 (2018) 6093–6101. https://doi.org/10.1016/j.ceramint.2018.12.083.

[18] M.K. M., M. Jagannatham, A.J. Berkmans, P. Haridoss, L.R. N., M. V. Shankar, Influence of pre-oxidation, versus post-oxidation of carbon nanohorns in TiO_2 nanohybrid for enhanced photocatalytic hydrogen production, Mater. Res. Bull. 109 (2018) 34–40. https://doi.org/10.1016/j.materresbull.2018.09.010.

[19] J. Bharatvaj, V. Preethi, S. Kanmani, Hydrogen production from sulphide wastewater using Ce^{3+}–TiO_2 photocatalysis, Int. J. Hydrogen Energy. 43 (2018) 3935–3945. https://doi.org/10.1016/j.ijhydene.2017.12.069.

[20] J. Huang, G. Li, Z. Zhou, Y. Jiang, Q. Hu, C. Xue, W. Guo, Efficient photocatalytic hydrogen production over Rh and Nb codoped TiO_2 nanorods, Chem. Eng. J. 337 (2017) 282–289. https://doi.org/10.1016/j.cej.2017.12.088.

[21] A. Sinhamahapatra, H.Y. Lee, S. Shen, S.S. Mao, J.S. Yu, H-doped TiO_{2-x} prepared with MgH_2 for highly efficient solar-driven hydrogen production, Appl. Catal. B Environ. 237 (2018) 613–621. https://doi.org/10.1016/j.apcatb.2018.06.030.

[22] S. Wei, S. Ni, X. Xu, A new approach to inducing Ti^{3+}in anatase $TiO_2$for efficient photocatalytic hydrogen production, Chinese J. Catal. 39 (2018) 510–516. https://doi.org/10.1016/S1872-2067(17)62968-1.

[23] W. Lei, G. Ziqian, L. Yuan, S. Houde, H. Jingwei, Y. Bingran, W. Qizhao, Photosensitization of CdS by acid red-94 modfied alginate: Dual ameliorative effect upon photocatalytic hydrogen evolution, Appl. Surf. Sci. 492 (2019) 598–606. https://doi.org/https://doi.org/10.1016/j.apsusc.2019.06.222.

[24] A. Boudjemaa, K. Bachari, M. Trari, Photo-electrochemical characterization of porous

material Fe-FSM-16. Application for hydrogen production, Mater. Sci. Semicond. Process. 16 (2013) 838–844. https://doi.org/10.1016/j.mssp.2013.01.008.

[25] H. Hentit, A. Boudjemaa, A. Bouchama, J.C. Jumas, K. Bachari, M.S. Ouali, Cobalt containing microporous aluminohosphates as new photocatalyst for hydrogen generation under visible irradiation, Mater. Res. Bull. 106 (2018) 418–427. https://doi.org/10.1016/j.materresbull.2018.06.025.

[26] B. Gilbert, C. Frandsen, E.R. Maxey, D.M. Sherman, Band-gap measurements of bulk and nanoscale hematite by soft x-ray spectroscopy, Phys. Rev. B - Condens. Matter Mater. Phys. 79 (2009) 1–7. https://doi.org/10.1103/PhysRevB.79.035108.

[27] A. Boudjemaa, S. Boumaza, M. Trari, R. Bouarab, A. Bouguelia, Physical and photo-electrochemical characterizations of α-Fe_2O_3. Application for hydrogen production, Int. J. Hydrogen Energy. 34 (2009) 4268–4274. https://doi.org/10.1016/j.ijhydene.2009.03.044.

[28] A. Boudjemaa, C. Daniel, C. Mirodatos, M. Trari, A. Auroux, R. Bouarab, In situ DRIFTS studies of high-temperature water-gas shift reaction on chromium-free iron oxide catalysts, Comptes Rendus Chim. 14 (2011) 534–538. https://doi.org/10.1016/j.crci.2010.11.007.

[29] A. Boudjemaa, M. Trari, Photo-catalytic hydrogen production over Fe_2O_3 based catalysts, Int. J. Hydrogen Energy. 35 (2010) 7684–7689. https://doi.org/10.1016/j.ijhydene.2010.05.096.

[30] H. Hentit, M.R. Ghezzar, M. Womes, J.C. Jumas, A. Addou, M.S. Ouali, Plasma-catalytic degradation of anthraquinonic acid green 25 in solution by gliding arc discharge plasma in the presence of tin containing aluminophosphate molecular sieves, J. Mol. Catal. A, Chem. 390 (2014) 37–44. https://doi.org/10.1016/j.molcata.2014.03.003.

[31] M.E. Davis, Ordered porous materials for emerging applications, Nature. 417 (2002)

813–821. https://doi.org/10.1038/nature00785.

[32] R.M. Irfan, T. Wang, D. Jiang, Q. Yue, L. Zhang, H. Cao, Y. Pan, P. Du, Highly Active Homogeneous Molecular Iron Catalysts for Direct Photocatalytic Conversion of Formic Acid to Syngas ($CO+H_2$) at Room Temperature by Visible Light, Angew. Chemie - Int. Ed. 59 (2020) 14818–14824. https://doi.org/10.1002/anie.202002757.

[33] C. A. Messina, B. M. Lok, E. M. Flanigen, U.S. Patent 4,544,143 (1985).

[34] B. M. Lok, C.A. Messina, R.L. Patton, R.T. Gajek, T. R. Cannan, E.M. Flanigen, U.S. Patent, 5,550,871 (1984).

[35] H. Hentit, K. Bachari, M.S. Ouali, M. Womes, B. Benaichouba, J.C. Jumas, Alkylation of benzene and other aromatics by benzyl chloride over iron-containing aluminophosphate molecular sieves, J. Mol. Catal. A Chem. 275 (2007) 158–166. https://doi.org/10.1016/j.molcata.2007.05.032.

[36] B. Liu, P. Jiang, P. Zhang, H. Zhao, J. Huang, Aluminum phosphate-based solid acid catalysts : Facile synthesis , characterization and their application in the esteri fi cation of propanoic acid with n -butanol, Comptes Rendus - Chim. 20 (2017) 540–548. https://doi.org/10.1016/j.crci.2016.07.006.

[37] S. Siliveri, S. Chirra, S. Goskula, S.R. Gujjula, V. Narayanan, Pd / SAPO-35 : Synthesis , characterization and its catalytic application studies on Suzuki-Miyaura Cross Coupling reaction, Mater. Today Proc. 45 (2021) 3778–3783. https://doi.org/10.1016/j.matpr.2021.01.277.

[38] D. Chandra, N. Kishor Mal, M. Mukherjee, A. Bhaumik, Titanium-rich highly ordered mesoporous silica synthesized by using a mixed surfactant system, J. Solid State Chem. 179 (2006) 1802–1807. https://doi.org/10.1016/j.jssc.2006.03.020.

[39] M.H. Zahedi-niaki, M.P. Kapoor, S. Kaliaguine, H_2O_2 Oxidation and Epoxidation of Hydrocarbons and Alcohols over Titanium Aluminophosphates TAPO-5, TAPO-11, and TAPO-36, J. Catal. 177 (1998) 231–239.

https://doi.org/https://doi.org/10.1006/jcat.1998.2127.

[40] N. Venkatathri, V.N. Shetty, Synthesis and characterization of TAPO-31 molecular sieves using tripropylamine template, Catal. Commun. 7 (2006) 1015–1021. https://doi.org/10.1016/j.catcom.2006.05.010.

[41] K. Leng, C. Zhang, X. Li, C. Hou, Y. Sun, Iron-containing MIL-101(Cr) as highly active and stable heterogeneous catalysts for the benzylation of aromatics with benzyl chloride, React. Kinet. Mech. Catal. 120 (2016) 345–357. https://doi.org/10.1007/s11144-016-1084-8.

[42] P. Wenqin, Q.I.U. Shilun, K.A.N. Qiubin, W.U. Zhiyun, P. Shaoyi, Synhesis and characterization of FAPO-5 crystallized from clear homogeneous solutions, Stud. Surf. Sci. Catal. 49 (1989) 281–289. https://doi.org/https://doi.org/10.1016/S0167-2991(08)61726-7.

[43] B. Notari, Microporous Crystalline Titanium Silicates, Adv. Catal. 41 (1996) 253–334. https://doi.org/10.1016/S0360-0564(08)60042-5.

[44] A. V Vijayasankar, N. Nagaraju, Preparation and characterisation of amorphous mesoporous aluminophosphate and metal aluminophosphate as an efficient heterogeneous catalyst for transesterification reaction, Comptes Rendus - Chim. 14 (2011) 1109–1116. https://doi.org/10.1016/j.crci.2011.09.013.

[45] G. Liu, Z. Wang, M. Jia, X. Zou, X. Zhu, W. Zhang, D. Jiang, Thermally stable amorphous mesoporous aluminophosphates with controllable P/Al ratio: Synthesis, characterization, and catalytic performance for selective O-methylation of catechol, J. Phys. Chem. B. 110 (2006) 16953–16960. https://doi.org/10.1021/jp062824u.

[46] A. Tuel, Synthesis, characterization, and catalytic properties of titanium silicoaluminophosphate TAPSO-5, Zeolites. 15 (1995) 228–235. https://www.nbk1560.com/en/products/specialscrew/nedzicom/titaniumscrew/point/.

[47] J.M. Campelo, M. Jaraba, D. Luna, R. Luque, J.M. Marinas, A.A. Romero, Effect of

Phosphate Precursor and Organic Additives on the Structural and Catalytic Properties of Amorphous Mesoporous AlPO 4 Materials, Chem. Mater. 15 (2003) 3352–3364. https://doi.org/https://doi.org/10.1021/cm030206+.

[48] Y.S. Kim, W.G. Choi, B.K. Ryu, Effect of ZnO Content Change on the Structure and Properties of Zinc Borophosphate Glasses 1, Glas. Phys. Chem. 40 (2014) 408–414. https://doi.org/10.1134/S1087659614040142.

[49] S.T. Reis et al, Structural features of lead iron phosphate glasses, J. Non. Cryst. Solids. 304 (2002) 188–194. https://doi.org/https://doi.org/10.1016/S0022-3093(02)01021-9.

[50] M.M. El-Desoky, A. Al-Hajry, M. Tokunaga, T. Nishida, M.Y. Hassaan, Effect of Sulfur Addition on the Redox State of Iron in Iron Phosphate Glasses, Hyperfine Interact. 156/157 (2004) 547–553. https://doi.org/10.1023/b:hype.0000043276.50691.16.

[51] A.K. Paul, M. Prabu, G. Madras, S. Natarajan, Effect of metal ion doping on the photocatalytic activity of aluminophosphates, J. Chem. Sci. 122 (2010) 771–785. https://doi.org/10.1007/s12039-010-0065-0.

[52] M.A. Zanjanchi, M.K. Rashidi, Structural charge transfer in the aluminophosphate molecular sieves by diffuse reflectance spectroscopy, Spectrochim. Acta - Part A Mol. Biomol. Spectrosc. 55 (1999) 947–954. https://doi.org/10.1016/S1386-1425(98)00207-8.

[53] M.A. Zanjanchi, A. Ghanadzadeh, F. Khadem-Nahvi, Incorporation of silicon into A1PO-5 framework sites: Higher thermal stability and lower extra-framework aluminum concentration, J. Incl. Phenom. 42 (2002) 295–299. https://doi.org/10.1023/A:1016015210310.

[54] A. Tuel, Y. Ben, Synthesis and Catalytic Properties of Titanium-substituted Silicoaluminophosphate TAPSO-5, J. CHEM. SOC., CHEM. COMMUN. (1994) 1667–1668. https://doi.org/https://doi.org/10.1039/C39940001667.

[55] E. Gianotti, A. Frache, S. Coluccia, J.M. Thomas, T. Maschmeyer, L. Marchese, The identity of titanium centres in microporous aluminophosphates compared with Ti-MCM-41 mesoporous catalyst and titanosilsesquioxane dimer molecular complex: a spectroscopy study, J. Mol. Catal. A Chem. 204–205 (2003) 483–489. https://doi.org/10.1016/S1381-1169(03)00330-3.

[56] J.W. Park, H. Chon, Isomorphous Substitution of Iron Ions into Aluminophosphate Molecular Sieve , $AlPO_4$-5, J. Catal. 133 (1992) 159–169. https://doi.org/https://doi.org/10.1016/0021-9517(92)90194-M.

[57] D. Goidfaib, M. Bernardo, K.G. Strohmaier, D.E.W. Vaughan, H. Thomann, Characterization of Iron in Zeolites by X-band and Q-Band ESR, Pulsed ESR, and UV-Visible Spectroscopies, J. Am. Chem. Soc. 116 (1994) 6344–6353. https://doi.org/10.1021/ja00093a039.

[58] S. Bordiga, R. Buzzoni, F. Geobaldo, C. Lamberti, E. Giamello, A. Zecchina, G. Leofanti, G. Petrini, G. Tozzola, G. Vlaic, Structure and reactivity of framework and extraframework iron in Fe-silicalite as investigated by spectroscopic and physicochemical methods, J. Catal. 158 (1996) 486–501. https://doi.org/10.1006/jcat.1996.0048.

[59] L. Wang, B. Tian, J. Fan, X. Liu, H. Yang, C. Yu, B. Tu, D. Zhao, Block copolymer templating syntheses of ordered large-pore stable mesoporous aluminophosphates and Fe-aluminophosphate based on an ‘“ acid – base pair ”’ route, Microporous Mesoporous Mater. 67 (2004) 123–133. https://doi.org/10.1016/j.micromeso.2003.11.007.

[60] J.A. Torres-Luna, N.R. Sanabria, J.G. Carriazo, Powders of iron(III)-doped titanium dioxide obtained by direct way from a natural ilmenite, Powder Technol. 302 (2016) 254–260. https://doi.org/10.1016/j.powtec.2016.08.056.

[61] J. Tauc, A. Menth, States in the gap, J. Non. Cryst. Solids. 8–10 (1972) 569–585.

https://doi.org/10.1016/0022-3093(72)90194-9.

[62] P.R. Jubu, F.K. Yam, V.M. Igba, K.P. Beh, Tauc-plot scale and extrapolation effect on bandgap estimation from UV–vis–NIR data – A case study of β-Ga_2O_3, J. Solid State Chem. 290 (2020) 121576. https://doi.org/10.1016/j.jssc.2020.121576.

[63] K. Persson, Materials Data on $ALPO_4$ (SG:82) by Materials Project, United States. (2014).

[64] H. Kenfoud, N. Nasrallah, O. Baaloudj, D. Meziani, T. Chaabane, M. Trari, Photocatalytic reduction of Cr(VI) onto the spinel $CaFe_2O_4$ nanoparticles, Optik (Stuttg). 223 (2020) 165610. https://doi.org/10.1016/j.ijleo.2020.165610.

[65] C. Guang-sen, M. Okido, T. Oki, Electrochemical studies of titanium ions (Ti^{4+}) in equimolar KClNaCl molten salts with 1 wt% K_2TiF_6, Electrochim. Acta. 32 (1987) 1637–1642. https://doi.org/10.1016/0013-4686(87)90017-X.

[66] G.Q. Liu, Y. Yang, Y. Li, L. Wu, Q. Xu, J. Zhu, S.H. Yu, Band Structure Engineering toward Low-Onset-Potential Photoelectrochemical Hydrogen Production, ACS Mater. Lett. 2 (2020) 1555–1560. https://doi.org/10.1021/acsmaterialslett.0c00424.

[67] R. Bagtache, I. Sebai, M. Trari, Visible light induced H_2 evolution on the hetero-junction Pt/$CuCo_2O_4$ prepared by hydrothermal route, Sol. Energy. 211 (2020) 971–976. https://doi.org/10.1016/j.solener.2020.10.046.

[68] I. Ghiat, A. Boudjemaa, A. Saadi, K. Bachari, N.J. Coville, Efficient hydrogen generation over a novel Ni phyllosilicate photocatalyst, J. Photochem. Photobiol. A Chem. 382 (2019) 111952. https://doi.org/https://doi.org/10.1016/j.jphotochem.2019.111952.

[69] Y. Zhou, Y. Qin, W. Dai, X. Luo. Highly Efficient Degradation of Tartrazine with a Benzoic Acid/TiO2 System. ACS Omega *4* (2019) 546-554. https://doi.org/10.1021/acsomega.8b03267

[70] T. Puangpetch, S. Chavadej, T. Sreethawong, Hydrogen production over Au-loaded mesoporous-assembled $SrTiO_3$ nanocrystal photocatalyst : Effects of molecular structure and chemical properties of hole scavengers, Energy Convers. Manag. 52 (2011) 2256–2261. https://doi.org/10.1016/j.enconman.2010.12.026.

[71] J.T. Schneider, D.S. Firak, R.R. Ribeiro, P.P.- Zamora, Use of scavenger agents in heterogeneous photocatalysis: truths, half-truths, and misinterpretations, Phys. Chem. Chem. Phys. 22 (2020) 15723–15733. https://doi.org/10.1039/D0CP02411B.

[72] Y. Sun and J. J. Pignatello, Evidence for a Surface Dual Hole- Radical Mechanism in the TiO_2 Photocatalytic Oxidation of 2,4D, Environ. Sci. Technol. 29 (1995) 2065–2072. https://doi.org/10.1021/es00008a028.

[73] Y. Matsumoto, Energy Positions of Oxide Semiconductors and Photocatalysis with Iron Complex Oxides, J. Solid State Chem. 126 (1996) 227–234. https://doi.org/https://doi.org/10.1006/jssc.1996.0333.

[74] J. Shivanand, M.K. Dongar, S.B. Kulkarni, Electrical Conductivity of Iron (III)-exchanged Y Zeolites, J. Chem. SOC. Furaday Trans. 77 (1981) 3019–3021. https://doi.org/http://pubs.rsc.org | doi:10.1039/F19817703019.